

# Low-energy enhancement and fluctuations of $\gamma$ -ray strength functions in $^{56,57}\text{Fe}$ : test of the Brink-Axel hypothesis

A. C. Larsen<sup>1</sup>, M. Guttormsen<sup>1</sup>, N. Blasi<sup>2</sup>, A. Bracco<sup>2,3</sup>,  
F. Camera<sup>2,3</sup>, L. Crespo Campo<sup>1</sup>, T. K. Eriksen<sup>1,4</sup>, A. G3rgen<sup>1</sup>,  
T. W. Hagen<sup>1</sup>, V. W. Ingeberg<sup>1</sup>, B. V. Kheswa<sup>1</sup>, S. Leoni<sup>2,3</sup>,  
J. E. Midtb3r<sup>1</sup>, B. Million<sup>2</sup>, H. T. Nyhus<sup>1</sup>, T. Renstr3m<sup>1</sup>,  
S. J. Rose<sup>1</sup>, I. E. Ruud<sup>1</sup>, S. Siem<sup>1</sup>, T. G. Tornyi<sup>1,4</sup>,  
G. M. Tveten<sup>1</sup>, A. V. Voinov<sup>5</sup>, M. Wiedeking<sup>6</sup>, and F. Zeiser<sup>1</sup>

E-mail: a.c.larsen@fys.uio.no

<sup>1</sup> Department of Physics, University of Oslo, N-0316 Oslo, Norway

<sup>2</sup> INFN, Sezione di Milano, Milano, Italy

<sup>3</sup> Dipartimento di Fisica, University of Milano, Milano, Italy

<sup>4</sup> Department of Nuclear Physics, Australian National University, Canberra, Australia

<sup>5</sup> Department of Physics and Astronomy, Ohio University, Athens, Ohio 45701, USA

<sup>6</sup> iThemba LABS, P.O. Box 722, 7129 Somerset West, South Africa

October 2016

**Abstract.** Nuclear level densities and  $\gamma$ -ray strength functions of  $^{56,57}\text{Fe}$  have been extracted from proton- $\gamma$  coincidences. The level densities are compared to previous experimental data, both from particle-evaporation spectra and  $^3\text{He}$ -induced reactions. The low-energy enhancement in the  $\gamma$ -ray strength functions, first discovered in  $(^3\text{He}, ^3\text{He}'\gamma)^{57}\text{Fe}$  and  $(^3\text{He}, \alpha\gamma)^{56}\text{Fe}$  data, is confirmed with the experiments reported here. Angular distributions of the low-energy enhancement in  $^{57}\text{Fe}$  indicate its dipole nature.

The high statistics and the excellent energy resolution of the large-volume  $\text{LaBr}_3(\text{Ce})$  detectors allowed for a thorough analysis of the  $\gamma$ -ray strength function as a function of excitation energy. Strong fluctuations were found for the direct decay to the ground band, while the decay into the quasi-continuum shows a more uniform behavior. There is no indication of any significant excitation-energy dependence in the  $\gamma$ -ray strength function, in support of the generalized Brink-Axel hypothesis.

PACS numbers: 21.10.Ma, 21.10.-k, 27.40.+z, 25.20.Lj

*Keywords:* Level density,  $\gamma$ -strength function, angular distributions, Brink hypothesis, iron

Submitted to: *J. Phys. G: Nucl. Phys.*

## 1. Introduction

One of the long-standing experimental and theoretical challenges within nuclear physics is the determination of the nucleus' available quantum levels and the decay properties of these levels in the excitation-energy region between the ground state and up to the particle threshold(s). In this intermediate excitation-energy region, often called the *quasicontinuum*, the *nuclear level density* (NLD) and the average, reduced  $\gamma$ -decay probability, i.e. the  $\gamma$ -*strength function* ( $\gamma\text{SF}$ ), shed light on the dynamic behavior of the nucleus. Apart from providing information on basic nuclear properties, these quantities are also indispensable input for calculations of, e.g., neutron-capture cross sections. These cross sections are of great importance for applications such as the astrophysical heavy-element nucleosynthesis [1, 2] and modeling of next-generation nuclear power plants [3, 4].

Amongst a handful of experimental techniques, the Oslo method [5] has been established as one of the promising approaches to obtain experimental information on the NLD and  $\gamma\text{SF}$ . The advantage of the Oslo method compared to other techniques is that both these quantities can be extracted from one and the same experiment, utilizing typically a charged-particle reaction to record particle- $\gamma$  coincidences, in which the structural shape of the NLD and the  $\gamma\text{SF}$  can be determined. By measuring the energy of the outgoing charged particle, the initial excitation energy of the residual nucleus is determined. The  $\gamma$  rays de-exciting this initial excitation energy are recorded in coincidence, thus obtaining  $\gamma$  spectra as function of initial excitation-energy.

In 2004, an unexpected enhancement of the  $\gamma\text{SF}$  for low transition energies ( $E_\gamma \lesssim 3$  MeV) was discovered in the iron isotopes  $^{56,57}\text{Fe}$  [6]. This feature was not predicted by any theoretically derived  $\gamma\text{SF}$ s. In the following years, this *upbend* was found in many medium-mass nuclei, including  $^{43-45}\text{Sc}$  [7, 8],  $^{60}\text{Ni}$  [9],  $^{73,74}\text{Ge}$  [10], and Mo isotopes [11, 12, 13]. To date, the heaviest nuclei where the upbend has been seen are  $^{138,139}\text{La}$  [14] and  $^{151,153}\text{Sm}$  [15]. The upbend was experimentally shown to be of dipole nature in  $^{56}\text{Fe}$  [16]. Moreover, it has been demonstrated [17] that such a low-energy enhancement in the  $\gamma\text{SF}$  could significantly increase radiative neutron-capture rates of relevance for the *r*-process – if found to be present in very neutron-rich nuclei.

In 2012, the upbend was independently confirmed in  $^{95}\text{Mo}$  [12] using a different technique. This triggered theoretical investigations of the origin of this phenomenon. Within the thermal-continuum quasiparticle random-phase approximation (TCQRPA), the upbend was explained as due to *E1* transitions caused by thermal single-quasiparticle excitations in the continuum [18], with its strength depending on the nuclear temperature. On the other hand, shell-model calculations [19, 20] show a strong increase in  $B(M1)$  strength for low-energy *M1* transitions. At present,  $^{60}\text{Ni}$  is the only case where experimental data favor a magnetic character of the upbend [9]. More experimental information is needed in order to determine whether the upbend is dominantly of magnetic or electric character, or a mixture of both.

In this work, we present NLDs and  $\gamma\text{SF}$ s of  $^{56,57}\text{Fe}$  extracted from  $(p,p'\gamma)$

coincidences. We analyze systematic errors in the normalization procedure and compare our results to available data in the literature. For the first time, we present angular distributions of the upbend in  $^{57}\text{Fe}$ , as well as  $\gamma$ SFs as function of excitation energy to investigate the so-called *generalized Brink-Axel hypothesis* for  $^{56,57}\text{Fe}$ . This hypothesis has up to now only been validated for the heavy nucleus  $^{238}\text{Np}$  [21].

This article is organized as follows. In section 2, we give experimental details and the main steps of the Oslo-method analysis. In section 3, the NLDs and  $\gamma$ SFs are shown and the normalization uncertainties are discussed. Further, in section 4 angular distributions are presented for  $^{57}\text{Fe}$ , while section 5 deals with  $\gamma$ SFs as function of excitation energy and implications for the generalized Brink-Axel hypothesis. Finally, a summary and outlook are given in section 6.

## 2. Experimental details and data analysis

The experiments were performed at the Oslo Cyclotron Laboratory (OCL). A 16-MeV proton beam with intensity of  $\approx 0.5$  nA impinging on self-supporting targets of 99.9% enriched  $^{56}\text{Fe}$  and 92.4% enriched  $^{57}\text{Fe}$ . Both targets had mass thickness of  $\approx 2$  mg/cm<sup>2</sup>. Accumulating times were  $\approx 85$ h and  $\approx 92$ h for  $^{56,57}\text{Fe}$ , respectively.

The charged ejectiles were measured with the Silicon Ring particle-detector system (SiRi) [22] and the  $\gamma$  rays with the CACTUS array [23]. The SiRi system consists of eight  $\Delta E - E$  telescopes. Each telescope is composed of a 130- $\mu\text{m}$  thick front detector segmented into eight strips (angular resolution of  $\Delta\theta \simeq 2^\circ$ ), and a 1550- $\mu\text{m}$  thick back detector. In total, SiRi has 64 individual detectors and a solid-angle coverage of  $\approx 6\%$ . For these experiments, SiRi was placed in forward angles with respect to the beam direction, covering  $40 - 54^\circ$ . From the measured energy of the ejectiles and the reaction kinematics, the excitation energy of the residual nucleus is deduced.

In this experiment, the CACTUS array contained 22 collimated 5 *in.*  $\times$  5 *in.* NaI(Tl) detectors and six collimated 3.5 *in.*  $\times$  8 *in.* LaBr<sub>3</sub>(Ce) detectors from the Milan HECTOR<sup>+</sup> array [24, 25]. The NaI detectors were placed on the CACTUS frame with six different angles  $\theta$  with respect to the beam direction (37.4, 63.4, 79.3, 100.7, 116.6, and 142.6 degrees), while the LaBr<sub>3</sub> crystals covered four angles (63.4, 79.3, 100.7, and 116.6 degrees). The  $\gamma$ -energy thresholds were  $\approx 400$  keV and  $\approx 800$  keV for the NaI and LaBr<sub>3</sub> detectors, respectively. Particle- $\gamma$  coincidences were recorded event-by-event, with the overlap of the  $\Delta E$  and  $E$  detectors of SiRi as mastergate for the analog electronics. In total, after background subtraction, about 65 million coincidences were obtained for the NaI detectors and about 12 million coincidences for the LaBr<sub>3</sub> detectors with the  $^{56}\text{Fe}$  target. Correspondingly, for  $^{57}\text{Fe}$ , about 15 million and 2.1 million coincidences were recorded for the NaI and LaBr<sub>3</sub> detectors, respectively.

In figure 1, the proton spectrum of SiRi in coincidence with  $\gamma$  rays from the present experiment is compared to the  $\alpha$  spectrum from the previous experiment reported in Ref. [6]. The significant improvement in energy resolution is clear; the proton spectra have a full width at half maximum (FWHM) of  $\approx 90$  keV compared to the  $\alpha$  spectra

where  $\text{FWHM} \approx 500$  keV.

The proton- $\gamma$  coincidence matrices for the NaI and LaBr<sub>3</sub> detectors are displayed in figure 2. The superior energy resolution for the LaBr<sub>3</sub> spectra relative to the NaI ones is evident, as well as diagonals for which the excitation energy  $E$  equals the  $\gamma$  energy  $E_\gamma$  corresponding to decay to the ground state. Other diagonals are also clearly visible, for example the direct decay to the first-excited  $2^+$  state in  $^{56}\text{Fe}$ .

It is also very interesting to note the "triangles" in the  $^{57}\text{Fe}$  matrix where the  $\gamma$  intensity suddenly drops, see for example at  $E_\gamma \approx E \approx 8.5$  MeV in figure 2c,d. One would naively think that the  $\gamma$  intensity would be significantly reduced as soon as the neutron separation energy  $S_n$  is reached; however, this is well above  $S_n = 7.646$  MeV. This feature is explained by considering the average spin  $\langle J \rangle$  populated at high excitation energies. From  $\gamma$  transitions in coincidence with protons, we identify the decay from the  $6^+$  level at  $E = 3.39$  MeV in  $^{56}\text{Fe}$  as well as other levels with spins 2, 3, 4, 5 [16]. Levels with these spins will be hindered in decaying through  $s$ -wave neutron emission to the  $0^+$  ground state in  $^{56}\text{Fe}$ . This hindrance is studied in detail for  $^{95}\text{Mo}$  and applied in a novel technique to determine spins in [26].

In order to obtain the correct  $\gamma$ -energy distribution for each excitation-energy bin, the signals from the NaI and LaBr<sub>3</sub> detectors must be corrected for the detector response. We applied the unfolding technique described in [27], which is an iterative procedure using a strong smoothing of the Compton part of the spectrum. In order to construct response functions for the NaI and LaBr<sub>3</sub> detectors, we used in-beam measured

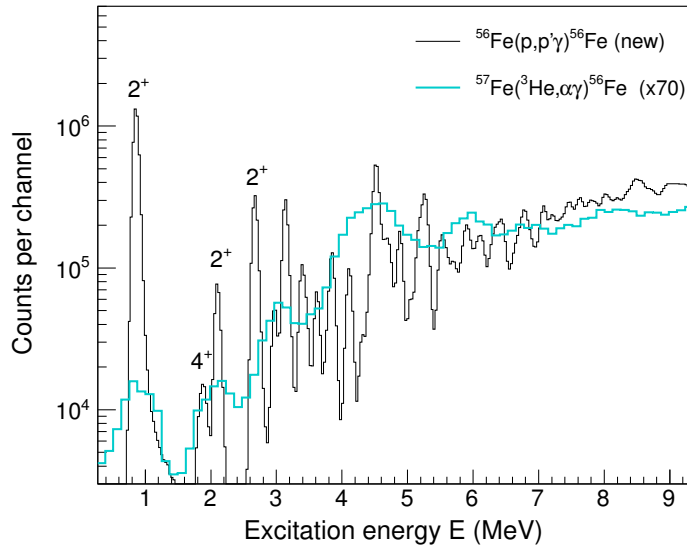


**Figure 1.** (Color online) Proton spectra (black histogram, this work) and  $\alpha$  spectra [6] (thick cyan line, scaled with a factor of 70) in coincidence with  $\gamma$  rays measured with the CACTUS NaI detectors for  $^{56}\text{Fe}$ . Energy bins are 31 keV/channel for protons and 123 keV/channel for  $\alpha$ s. The first excited levels are marked with their spin/parity.

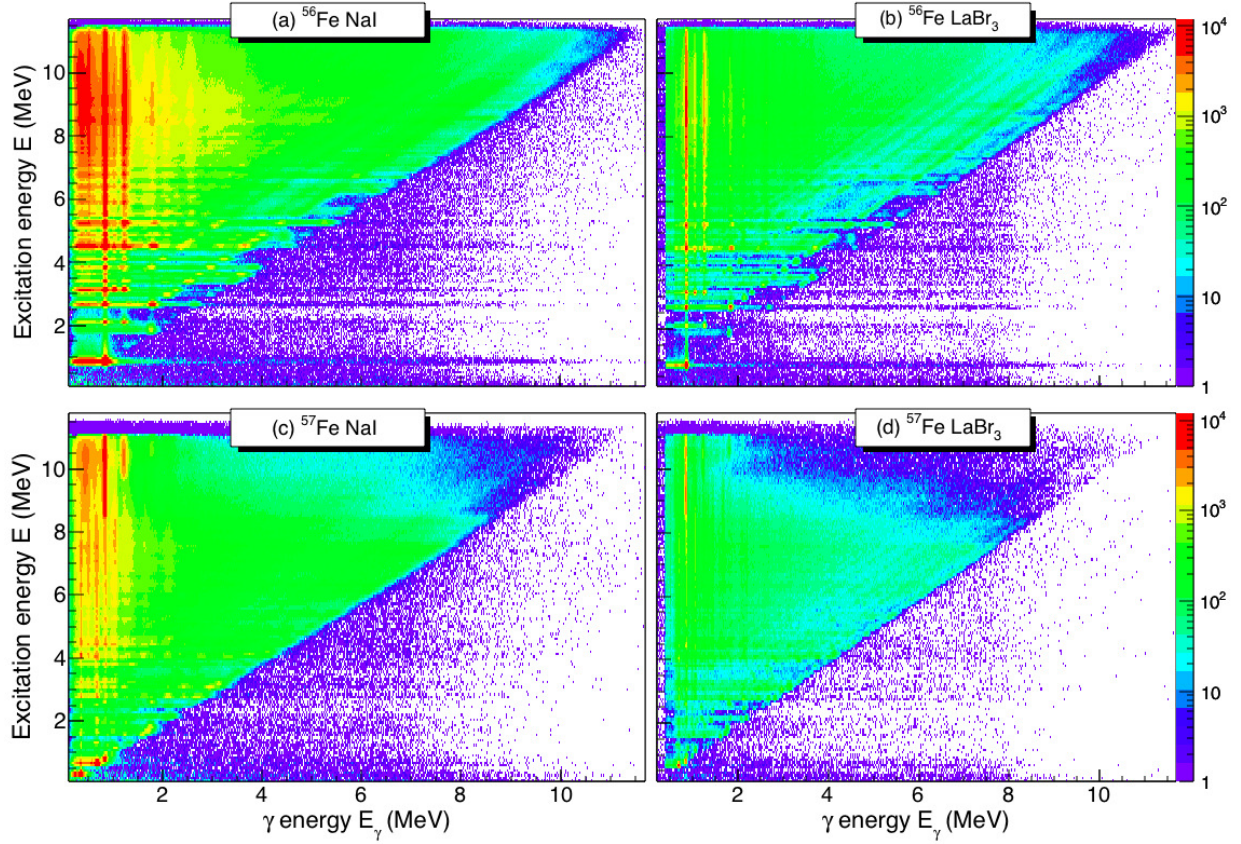


**Figure 2.** (Color online)  $\gamma$ -ray energy versus excitation energy before unfolding for (a)  $^{56}\text{Fe}$ , NaI detectors; (b)  $^{56}\text{Fe}$ , LaBr<sub>3</sub> detectors; (c)  $^{57}\text{Fe}$ , NaI detectors; (d)  $^{57}\text{Fe}$ , LaBr<sub>3</sub> detectors. Energy bins are 14 keV/channel.

transitions from  $^{56}\text{Fe}$ ,  $^{28}\text{Si}$ ,  $^{13}\text{C}$ , and  $^{16}\text{O}$  [28]. Moreover, we made use of a subtraction technique [29] to extract the distribution of primary  $\gamma$  rays for each excitation-energy bin. This distribution contains information on the NLD and the  $\gamma\text{SF}$  as deduced from Fermi's Golden Rule [30, 31]:

$$\lambda = \frac{2\pi}{\hbar} |\langle f | H' | i \rangle|^2 \rho_f, \quad (1)$$

where  $\lambda$  is the decay rate between initial state  $i$  and final state  $f$ ,  $H'$  is the transition operator and  $\rho_f$  is the density of final states. Similarly, the distribution of primary  $\gamma$  rays as function of  $E$  depends on the level density at  $E_f = E - E_\gamma$  and the  $\gamma$ -transmission coefficient  $\mathcal{T}$  for the  $\gamma$  transition with energy  $E_\gamma$ . The  $\gamma$ -transmission coefficient is directly proportional to the  $\gamma\text{SF}$ . Our ansatz is [5]:

$$P(E_\gamma, E) \propto \rho(E_f) \mathcal{T}(E_\gamma), \quad (2)$$

where  $P(E_\gamma, E)$  is the matrix of primary  $\gamma$  rays, representing relative intensities or branching ratios for a given transition energy  $E_\gamma$  at a given initial excitation energy  $E$ .

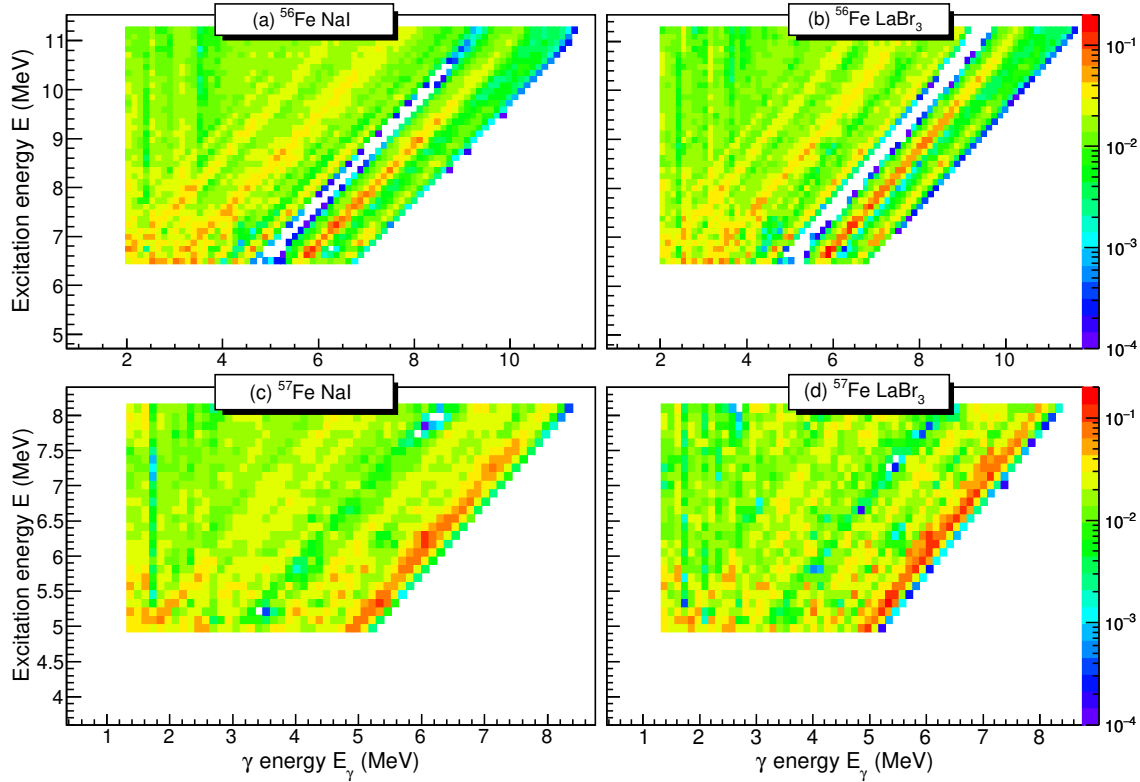


**Figure 3.** (Color online) Distribution of primary  $\gamma$  rays energy versus excitation energy for (a)  $^{56}\text{Fe}$ , NaI detectors; (b)  $^{56}\text{Fe}$ ,  $\text{LaBr}_3$  detectors; (c)  $^{57}\text{Fe}$ , NaI detectors; (d)  $^{57}\text{Fe}$ ,  $\text{LaBr}_3$  detectors. Energy bins are 124 keV/channel for  $^{56}\text{Fe}$  and 120 keV/channel for  $^{57}\text{Fe}$ . Note the different energy scales for the lower and upper panels.

The primary  $\gamma$ -ray matrices  $P(E_\gamma, E)$  for  $^{56,57}\text{Fe}$  are shown in figure 3. They are normalized for each excitation-energy bin so that  $\sum_{E_\gamma} P(E_\gamma, E) = 1$ . This means that the probability for  $\gamma$  decay from a given bin is 1, and that the intensity of a given  $\gamma$ -ray energy reflects the branching ratio for that particular transition energy.

These matrices are used as input for the extraction of the NLD and  $\gamma$ SF for the four data sets. The expression in equation 2 is valid for statistical decay, i.e. where the decay is independent of the formation of the compound state [34]. This is fulfilled at rather high excitation energies where the initial NLD is high, typically above  $\approx 2\Delta$  where the pair-gap parameter  $\Delta \approx 12A^{-1/2}$  [34]. Note that  $\mathcal{T}$  is a function only of  $E_\gamma$  and not  $E$  or  $E_f$ , in accordance with the generalized Brink-Axel hypothesis [32, 33]. This will be discussed in detail in section 5.

The functional form of the NLD and  $\gamma$ SF is determined through a least- $\chi^2$  fit to the  $P(E_\gamma, E)$  matrices as described in [5]. The 3D landscapes as shown in figure 3 are used simultaneously in the fit. The sum of all primary transitions for each  $E$  bin is normalized to unity. As the  $P(E_\gamma, E)$  matrices contain many more data points ("pixels") than the free parameters (the vector elements of  $\rho(E_f)$  and  $\mathcal{T}(E_\gamma)$ ), the solution is uniquely

determined and the fit routine converges fast, typically within 10-20 iterations.

Some considerations need to be made before extracting the NLD and  $\gamma$ SF from the data. First, a low-energy limit for the excitation energy is applied to avoid the discrete region at low  $E$ , for which the condition of a compound-nucleus decay is highly questionable. Further, an upper limit  $E_{\text{max}}$  must be given, which typically corresponds to  $S_n$ , as neutrons are not measured or discriminated in the present experimental setup. Finally, a low-energy limit on the  $\gamma$  energy,  $E_{\gamma,\text{low}}$ , is determined to exclude eventual higher-generation transitions not properly subtracted in the primary-distribution extraction, as discussed in detail in [35]. The chosen energy limits for the extraction procedure are:  $E_{\gamma,\text{low}} = 2.1$  MeV,  $E_{\text{min}} = 6.6$  MeV, and  $E_{\text{max}} = 11.3$  MeV for  $^{56}\text{Fe}$ ; correspondingly,  $E_{\gamma,\text{low}} = 1.4$  MeV,  $E_{\text{min}} = 5.0$  MeV, and  $E_{\text{max}} = 8.2$  MeV for  $^{57}\text{Fe}$ . The neutron separation energies  $S_n$  are 11.197 MeV and 7.646 MeV for  $^{56,57}\text{Fe}$ , respectively. The reason why we are able to put  $E_{\text{max}}$  higher than  $S_n$  in the case of  $^{57}\text{Fe}$ , is that the first-excited state in  $^{56}\text{Fe}$  is at 847 keV, allowing in principle for  $E_{\text{max}} = (7.65 + 0.85)$  MeV = 8.5 MeV as we are requiring proton- $\gamma$  coincidences. Similarly, for  $^{57}\text{Fe}$ , the upper limit is  $\approx 100$  keV above  $S_n$ .

To test the quality of the fit, which is based on all primary spectra included in the extraction procedure, we take the obtained  $\rho(E_f)$  and  $\mathcal{T}(E_\gamma)$  functions and use them to generate primary  $\gamma$  spectra to be compared with the input spectra bin by bin. This is shown in figure 4. Error bars in the primary spectra reflect statistical uncertainties, and systematic uncertainties stemming from the unfolding procedure and the extraction of the primary  $\gamma$  rays [5].

As can be seen from figures 4–7, the overall agreement between the data and the calculated primary spectra is very good. It should be noted that Porter-Thomas fluctuations [36] of the decay strengths are not taken into account. These fluctuations are expected to be large when the final level density  $\rho_f$  is low. This is clearly visible *e.g.* in the decay to the first-excited level in  $^{56}\text{Fe}$ , see figure 4a and the peak at  $E_\gamma \approx 6.5$  MeV, where data points are several standard deviations off the calculated  $\rho \times \mathcal{T}$ . Here, there is only one final level and the relative decay strength is seen to fluctuate strongly for different initial excitation energies.

### 3. Level density and $\gamma$ strength

#### 3.1. Normalization

As only the functional form of the NLD and  $\gamma$ SF can be deduced from the primary  $\gamma$  spectra, the slope and absolute normalization must be determined from auxiliary data. It is shown in [5] that any solution  $\tilde{\rho}_f$  and  $\tilde{\mathcal{T}}$  will give an equally good  $\chi^2$  fit to the primary- $\gamma$  data through the transformations

$$\rho(E - E_\gamma) = \mathcal{A} \exp[\alpha(E - E_\gamma)] \tilde{\rho}(E - E_\gamma), \quad (3)$$

$$\mathcal{T}(E_\gamma) = \mathcal{B} \exp(\alpha E_\gamma) \tilde{\mathcal{T}}(E_\gamma), \quad (4)$$



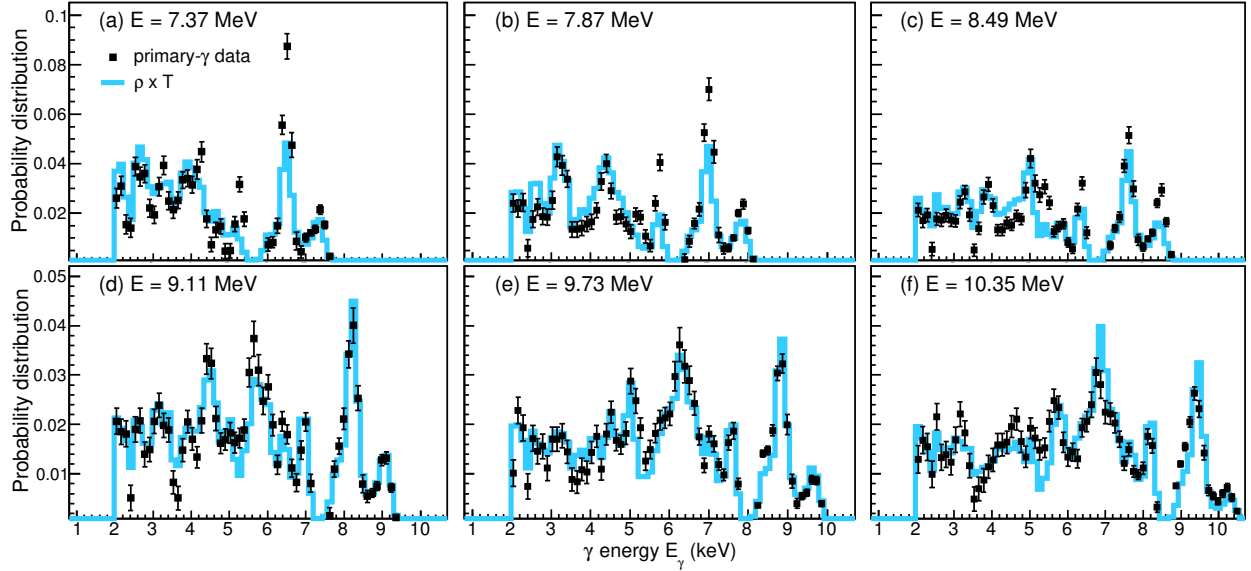


**Figure 4.** (Color online) Comparison of experimental primary  $\gamma$  spectra for  $^{56}\text{Fe}$  (black points, NaI detectors) with the calculated ones (blue histogram) from the extracted  $\rho$  and  $\mathcal{T}$  functions for a set of initial excitation-energy bins as indicated in the panels. Energy bins are 124 keV/channel.

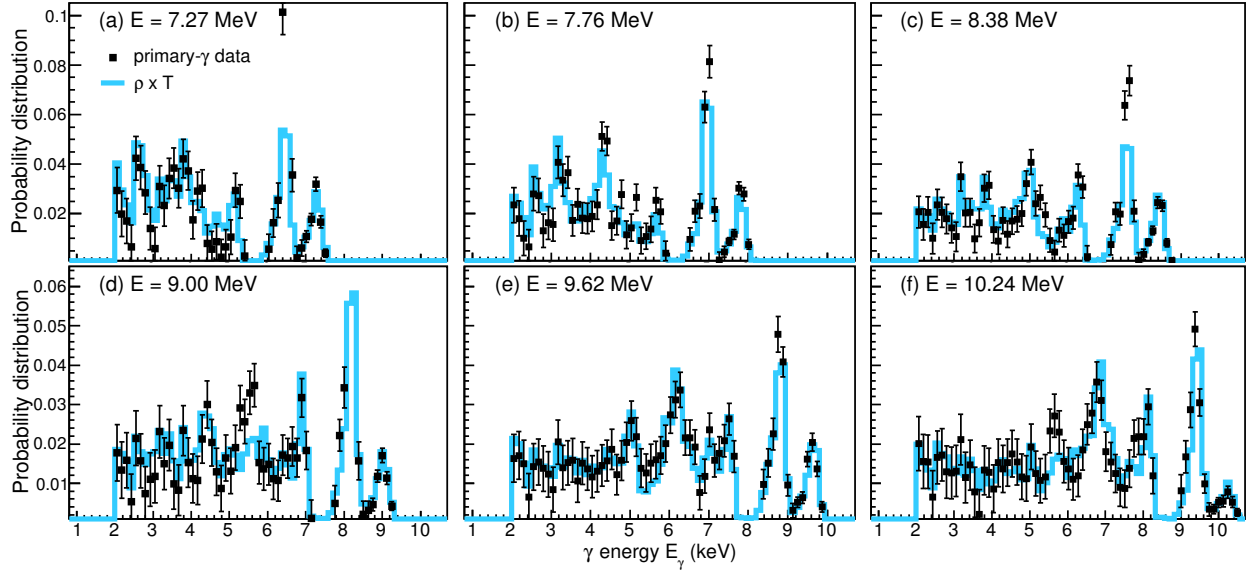


**Figure 5.** (Color online) Same as figure 4 for  $^{56}\text{Fe}$ , using data from the  $\text{LaBr}_3$  detectors.

where the parameters  $\mathcal{A}$ ,  $\mathcal{B}$ , are the absolute normalization of the NLD and the  $\gamma$ -transmission coefficient, respectively, and  $\alpha$  is the common slope parameter.

For the NLD, the parameters  $\mathcal{A}$  and  $\alpha$  are found by fitting our data to known



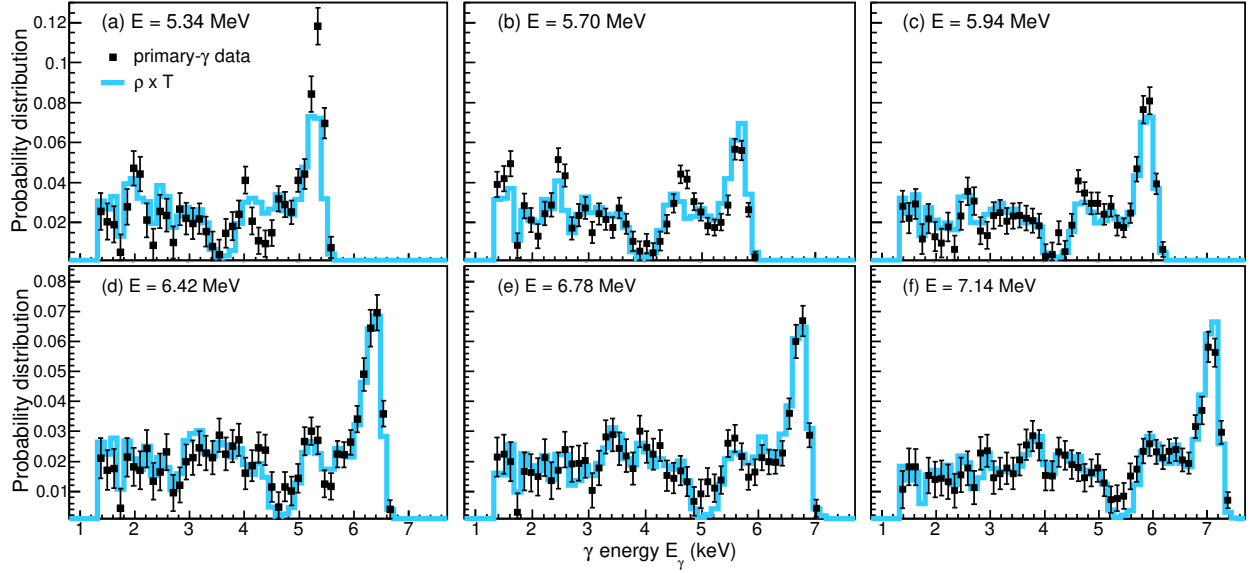


**Figure 6.** (Color online) Same as figure 4 for  $^{57}\text{Fe}$  measured with NaI detectors. Energy bins are 120 keV/channel.

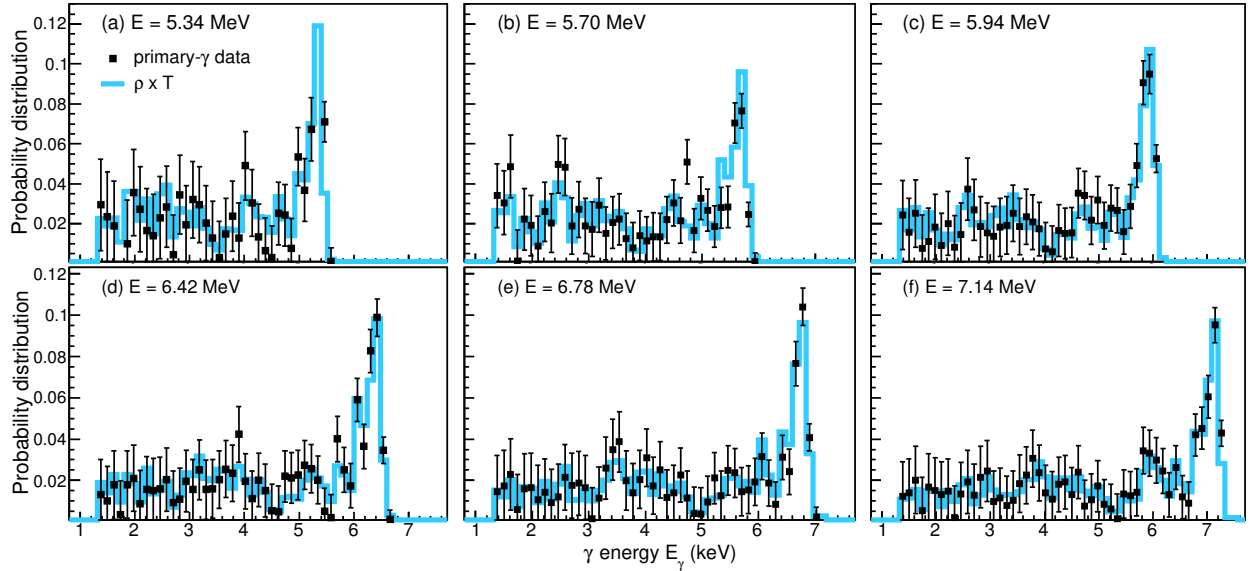


**Figure 7.** (Color online) Same as figure 4 for  $^{57}\text{Fe}$  using data from the LaBr<sub>3</sub> detectors.

levels from the literature [37] at low excitation energy and to neutron-resonance spacing data from [38] at  $S_n$ . The discrete levels are binned with the same bin width as our experimental data. For  $^{56}\text{Fe}$ , there is no information from neutron-resonance experiments as  $^{55}\text{Fe}$  is unstable. For this case, we have estimated the NLD at  $S_n$  from systematics in the following way:

- (i) To estimate the lower-limit NLD, we calculate the total level density from the  $s$ -wave neutron resonance spacing  $D_0$  for Fe isotopes where this value is available from [38] according to the expression

$$\rho(S_n) = \frac{2\sigma^2}{D_0} \cdot \frac{1}{(J_t + 1) \exp[-(J_t + 1)^2/2\sigma^2] + J_t \exp[-J_t^2/2\sigma^2]}, \quad (5)$$

assuming equally many positive- and negative-parity states. Here,  $J_t$  is the ground-state spin of the target nucleus in the neutron-resonance experiment and  $\sigma$  is the spin cutoff parameter. We make use of the phenomenological spin cutoff parameter suggested in [40]:

$$\sigma^2(E) = 0.391A^{0.675}(E - 0.5Pa')^{0.312}. \quad (6)$$

Here,  $A$  is the mass number and  $Pa'$  is the deuteron pairing energy as defined in [40]. This approach gives a low value for the spin cutoff parameter and thus a low limit for the level density. Further, we calculate  $\rho(S_n)$  from the global systematics [40] directly. By taking the  $\chi^2$  fit of the semi-experimental  $\rho(S_n)$  with the values from systematics in the same fashion as done for  $^{89}\text{Y}$  in [39], one obtains an estimate for the  $^{56}\text{Fe}$   $\rho_{\text{low}}(S_n)$ . All parameters are given in table 1. This normalization is referred to as *norm-1* in the following.

- (ii) To estimate the upper-limit NLD, we apply the same procedure as in (i) but with the spin cutoff parameter given by the rigid-body moment of inertia approach as parameterized in [41]:

$$\sigma^2(E) = 0.0146A^{5/3} \frac{1 + \sqrt{1 + 4a(E - E_1)}}{2a}. \quad (7)$$

Here,  $a$  is the level-density parameter and  $E_1$  is the excitation-energy backshift determined from global systematics of [41]. All parameters are given in table 2. We refer to this normalization as *norm-2*.

For  $^{57}\text{Fe}$ , we use the  $D_0$  value given in [38] and estimate  $\rho(S_n)$  using equation 5, again with spin cutoff parameters both from [40] and [41]. Consistent with the approach for  $^{56}\text{Fe}$ , the lower limit is obtained with the spin cutoff parameter in equation 6, and the upper limit with the one in equation 7, also including the uncertainties in  $D_0$ . All parameters are listed in table 1 and 2.

As our data reach up to  $E_{\text{max}} - E_{\gamma, \text{low}}$ , we must interpolate between the estimated  $\rho(S_n)$  and our upper data points. This is done using the constant-temperature formula of Ericson [42, 43]:

$$\rho_{CT}(E) = \frac{1}{T} \exp \frac{E - E_0}{T}. \quad (8)$$

The applied parameters  $T$  and  $E_0$  are given in table 3 for the various normalization options, giving the best fit to our data in the regions  $E = 8.2\text{--}9.2$  MeV and  $E = 6.2\text{--}6.6$  MeV for  $^{56,57}\text{Fe}$ , respectively. The normalized level densities are shown in figure 8.

With the normalized NLDs at hand, and assuming equal parity [44], we normalize the  $\gamma$ -ray transmission coefficient  $\mathcal{T}$  to the average, total radiative width  $\langle \Gamma_{\gamma 0} \rangle$  taken

**Table 1.** Neutron resonance parameters  $D_0$  and  $\langle\Gamma_{\gamma 0}\rangle$  from [38], and spin cutoff parameters from global systematics of [40];  $A_f$  is the final nucleus following neutron capture,  $J_t$  is the ground-state spin of the target nucleus,  $S_n$  is the neutron-separation energy,  $D_0$  is the  $s$ -wave level spacing [38],  $\sigma$  is the spin-cutoff parameter from equation (6),  $Pa'$  is the deuteron shift as defined in [40], and  $\rho(S_n)$  is the total level density calculated from equation 5. Finally,  $\rho^{\text{syst}}$  is the total level density at  $S_n$  as predicted from the global systematics of [40].  $^\dagger$ Estimated from systematics.

$A_f$	$J_t$	$S_n$ (MeV)	$D_0$ (keV)	$\sigma(S_n)$	$Pa'$ (MeV)	$\rho(S_n)$ ( $10^3 \text{ MeV}^{-1}$ )	$\rho^{\text{syst}}(S_n)$ ( $10^3 \text{ MeV}^{-1}$ )	$\langle\Gamma_{\gamma 0}\rangle$ (meV)
$^{55}\text{Fe}$	0	9.298	20.5(14)	3.41	0.463	1.19(9)	1.28	1600(700)
$^{56}\text{Fe}$	3/2	11.197	3.36(124) $^\dagger$	3.47	2.905	2.18(59) $^\dagger$	2.94	1900(600) $^\dagger$
$^{57}\text{Fe}$	0	9.298	25.4(22)	3.35	0.211	0.926(80)	1.14	920(410)
$^{58}\text{Fe}$	1/2	10.044	7.05(70)	3.44	2.874	1.81(18)	3.49	1850(500)
$^{59}\text{Fe}$	0	6.581	21.6(26)	3.30	0.470	1.06(13)	1.01	1130(110)

**Table 2.** Neutron resonance parameters  $D_0$  from [38], and spin cutoff parameters from global systematics of [41];  $A_f$  is the final nucleus following neutron capture,  $J_t$  is the ground-state spin of the target nucleus,  $S_n$  is the neutron-separation energy,  $\sigma$  is the spin-cutoff parameter from equation (7),  $D_0$  is the  $s$ -wave level spacing [38],  $a$  and  $E_1$  are the level density parameter and energy shift from [41], and  $\rho(S_n)$  is the total level density calculated from equation 5. Finally,  $\rho^{\text{syst}}$  is the total level density at  $S_n$  as predicted from the global systematics of [41].  $^\dagger$ Estimated from systematics.

$A_f$	$J_t$	$S_n$ (MeV)	$D_0$ (keV)	$\sigma(S_n)$	$a$ (1/MeV)	$E_1$ (MeV)	$\rho(S_n)$ ( $10^3 \text{ MeV}^{-1}$ )	$\rho^{\text{syst}}(S_n)$ ( $10^3 \text{ MeV}^{-1}$ )
$^{55}\text{Fe}$	0	9.298	20.5(14)	4.02	5.817	-0.524	1.62(11)	2.00
$^{56}\text{Fe}$	3/2	11.197	3.30 $^{+0.9}_{-0.6}$ $^\dagger$	4.05	6.196	0.942	2.87(68) $^\dagger$	4.22
$^{57}\text{Fe}$	0	9.298	25.4(22)	3.83	6.581	-0.523	1.20(10)	1.62
$^{58}\text{Fe}$	1/2	10.044	7.05(70)	3.93	6.936	0.942	2.32(23)	4.66
$^{59}\text{Fe}$	0	6.581	21.6(26)	3.70	7.297	-0.424	1.32(16)	1.38

**Table 3.** Parameters for the constant-temperature interpolation for the different normalization options. Both parameters  $T$  and  $E_0$  are given in MeV.

Nucleus	Norm-1						Norm-2					
	Lower		Middle		Upper		Lower		Middle		Upper	
	$T$	$E_0$	$T$	$E_0$	$T$	$E_0$	$T$	$E_0$	$T$	$E_0$	$T$	$E_0$
$^{56}\text{Fe}$	1.41	0.320	1.40	-0.034	1.38	-0.169	1.40	-0.070	1.35	0.045	1.30	0.232
$^{57}\text{Fe}$	1.32	-1.618	1.30	-1.575	1.29	-1.601	1.31	-1.882	1.29	-1.829	1.28	-1.848

from [38] (see table 1) according to [44]

$$\begin{aligned}
\langle\Gamma_{\gamma 0}(S_n, J_t \pm 1/2, \pi_t)\rangle &= \frac{\mathcal{B}}{4\pi\rho(S_n, J_t \pm 1/2, \pi_t)} \int_{E_\gamma=0}^{S_n} dE_\gamma \mathcal{T}(E_\gamma) \\
&\times \rho(S_n - E_\gamma) \sum_{J=-1}^1 g(S_n - E_\gamma, J_t \pm 1/2 + J), \quad (9)
\end{aligned}$$

where  $J_t$  and  $\pi_t$  are the spin and parity of the target nucleus in the  $(n, \gamma)$  reaction and

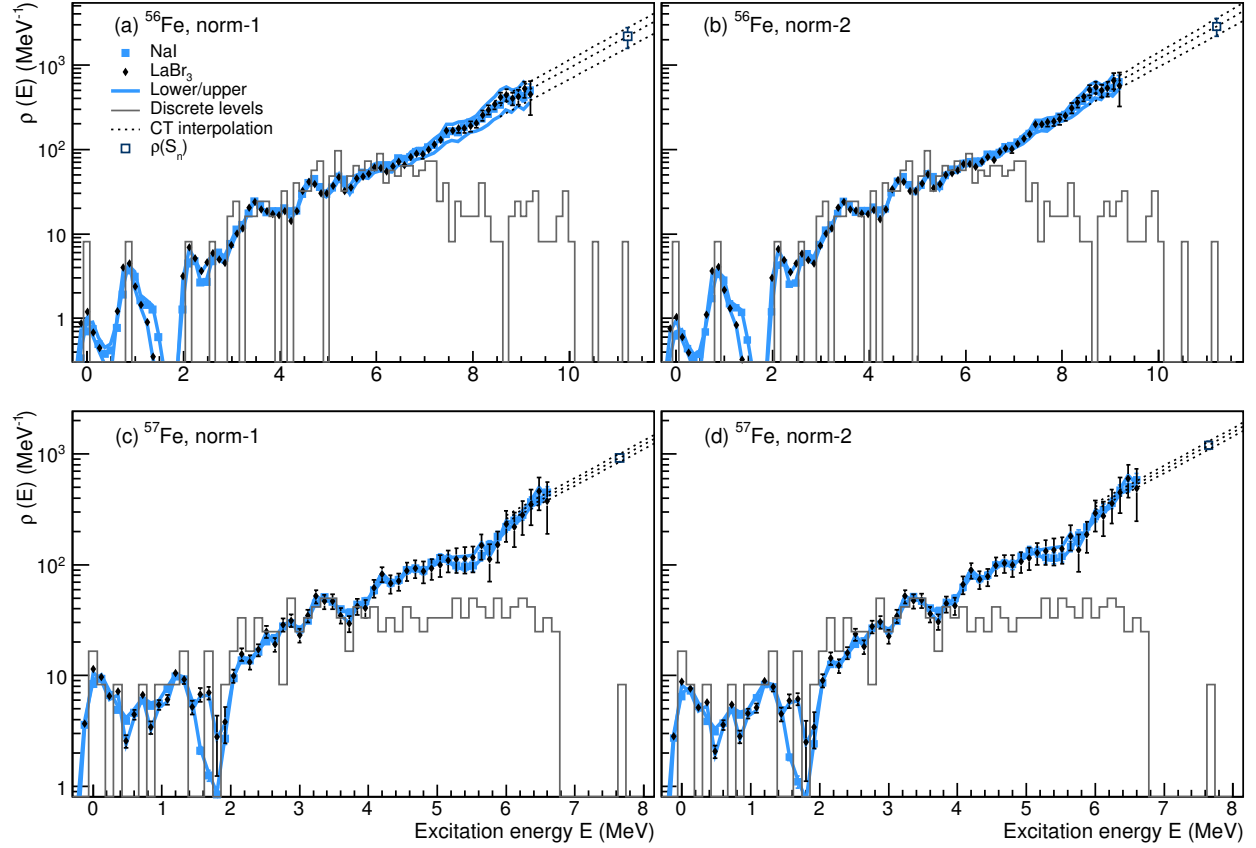


**Figure 8.** (Color online) Normalized level densities for (a)  $^{56}\text{Fe}$ , norm-1, (b)  $^{56}\text{Fe}$ , norm-2, (c)  $^{57}\text{Fe}$ , norm-1, and (d)  $^{57}\text{Fe}$ , norm-2.

$\rho(S_n - E_\gamma)$  is the experimental NLD. Note that the experimental transmission coefficient in principle includes all types of electromagnetic transitions:  $\mathcal{T}_{E1} + \mathcal{T}_{M1} + \mathcal{T}_{E2} + \dots$ ; however, dipole transitions are found to be dominant for decay in the quasicontinuum (e.g., [16, 45]). The sum in equation 9 runs over all final states with spins  $J_t \pm 1/2 + J$ , where  $J = -1, 0, 1$  from considering the spins reached after one primary dipole transition with energy  $E_\gamma$  (see also equation 3.1 in [45]). Note that the factor  $1/\rho(S_n, J_t \pm 1/2, \pi_t)$  equals the neutron resonance spacing  $D_0$ . From the normalized transmission coefficient, the  $\gamma$ SF is determined by

$$f(E_\gamma) = \frac{\mathcal{T}(E_\gamma)}{2\pi E_\gamma^3}. \quad (10)$$

Again,  $^{56}\text{Fe}$  lacks neutron resonance data and we have therefore estimated  $\langle \Gamma_{\gamma 0} \rangle$  from a linear fit to the values of the other Fe isotopes taken from [38], see table 1. The normalized  $\gamma$ SFs for the different normalization options for the level densities are shown in figure 9. The error band includes uncertainties in  $D_0$ , spin cutoff parameters, and  $\langle \Gamma_{\gamma 0} \rangle$ . We see that the  $\gamma$ SFs have a distinct U-like shape, independent on the choice of normalization. There is a characteristic increase in strength at low transition energies,

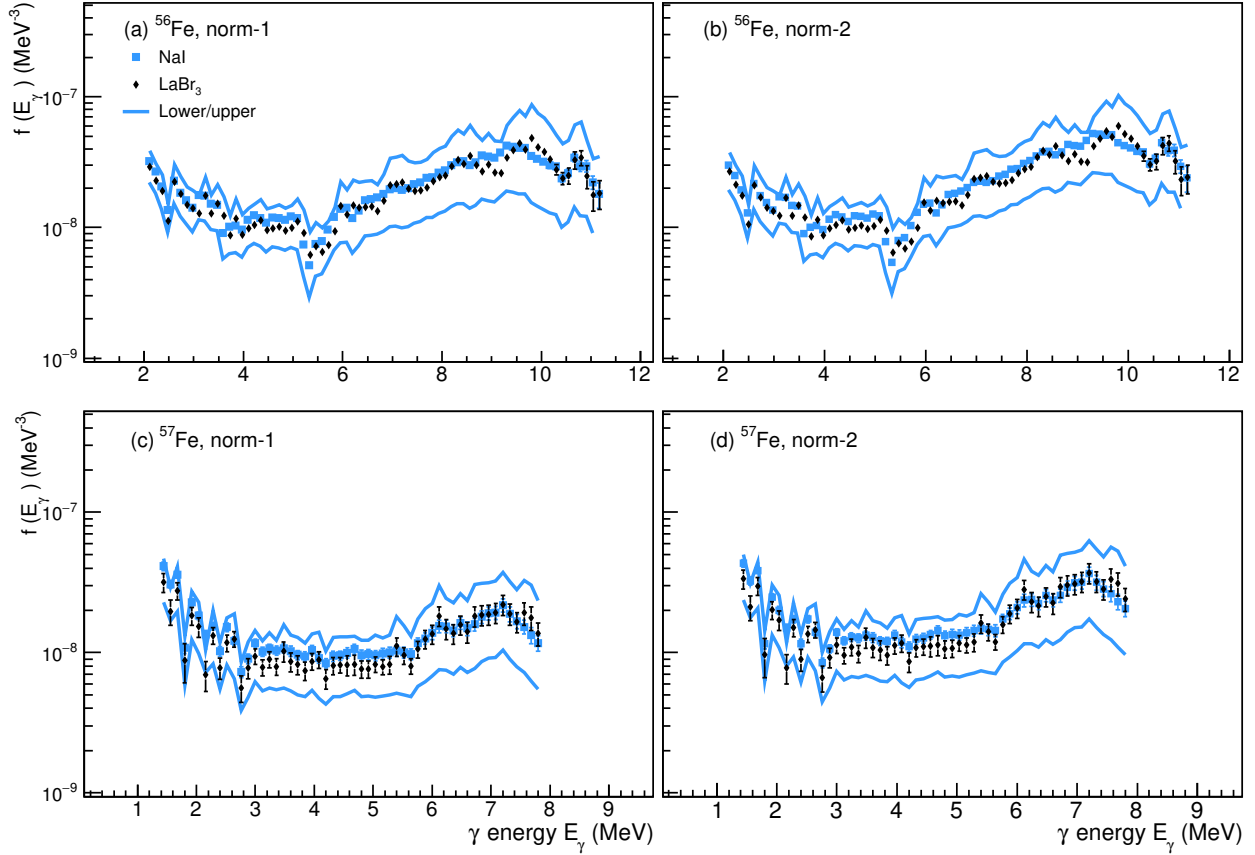


**Figure 9.** (Color online) Normalized  $\gamma$ SFs for (a)  $^{56}\text{Fe}$ , norm-1, (b)  $^{56}\text{Fe}$ , norm-2, (c)  $^{57}\text{Fe}$ , norm-1, and (d)  $^{57}\text{Fe}$ , norm-2.

which is very similar in shape and magnitude to recent predictions from large-scale shell-model calculations [20].

At the highest  $\gamma$ -ray energies, we observe a drop in strength, which could be due to the reaction populating spins at high excitation energies that on average are higher than the (close-to) ground-state spin(s), and/or a small overlap with the wave functions for the initial and final levels. In particular, for  $^{56}\text{Fe}$ , only  $1^-$  and  $1^+$  levels contribute to the dipole strength to the ground state. For lower transition energies, a broad range of levels is available as the final level density is much higher. One should therefore note that the upper data points ( $E_\gamma > 9.5$  and  $7.2$  MeV for  $^{56,57}\text{Fe}$ , respectively) do not represent a general, averaged  $\gamma$ SF in the quasicontinuum. The rather peculiar behavior of these data points indicate a possible (strong) dependence on the initial and final level(s), as well as significant Porter-Thomas fluctuations. This will be further investigated and discussed in section 5.

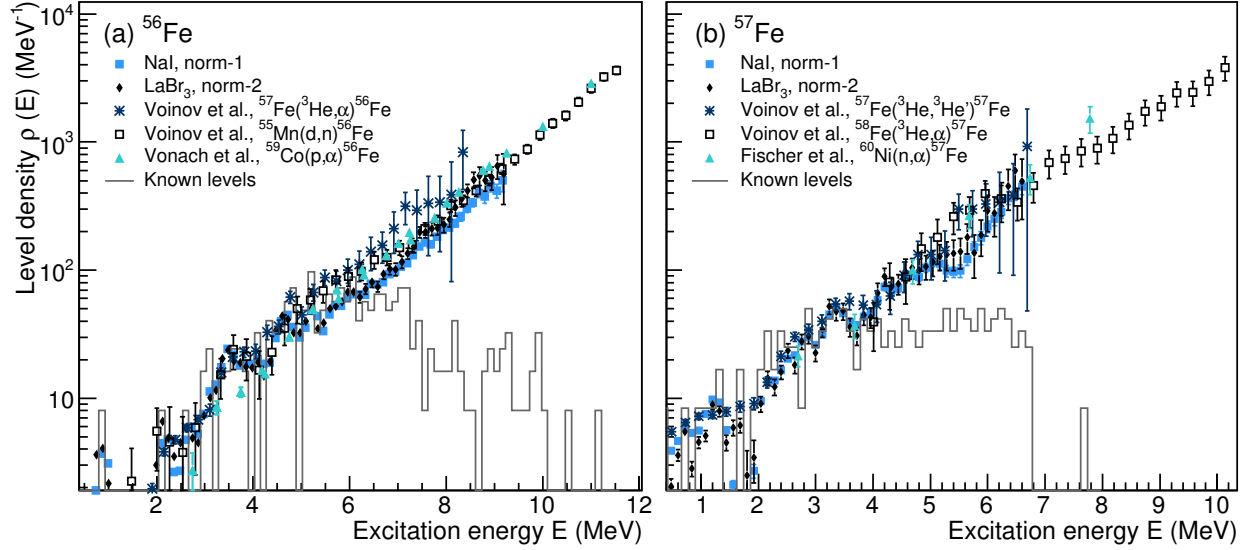


**Figure 10.** (Color online) Comparison of NLDs from different reactions for (a)  $^{56}\text{Fe}$  and (b)  $^{57}\text{Fe}$ . Previous data taken from [6, 46, 47, 48, 49].

### 3.2. Comparison with other data

There exist data on the NLDs of  $^{56,57}\text{Fe}$  from previous experiments at the OCL [6], using the  $^3\text{He}$ -induced reactions  $^{57}\text{Fe}(^3\text{He}, \alpha\gamma)^{56}\text{Fe}$  and  $^{57}\text{Fe}(^3\text{He}, ^3\text{He}'\gamma)^{57}\text{Fe}$ . Moreover, level densities have also been inferred from particle-evaporation spectra of the reactions  $^{55}\text{Mn}(d, n)^{56}\text{Fe}$  [46],  $^{59}\text{Co}(p, \alpha)^{56}\text{Fe}$  [47],  $^{58}\text{Fe}(^3\text{He}, \alpha)^{57}\text{Fe}$  [48], and  $^{60}\text{Ni}(n, \alpha)^{57}\text{Fe}$  [49]. Figure 10 shows the comparison of the present data and previous results. We find that the overall agreement is very good, although there are some differences between the data sets. For  $^{56}\text{Fe}$ , the absolute normalization is rather uncertain due to the lack of neutron-resonance data as discussed before; however, there is a significant boost in the number of levels at  $E \approx 6$  MeV for all data sets relative to the known, discrete levels. For  $^{57}\text{Fe}$ , a similar increase is taking place at  $E \approx 4$  MeV.

For the  $\gamma\text{SF}$ , there are to our knowledge no other data available for  $^{56,57}\text{Fe}$  neither below nor above the neutron separation energy, except for the previous  $^3\text{He}$ -induced reactions [6]. We have therefore compared our data to photoneutron ( $\gamma, n$ ) cross sections of  $^{55}\text{Mn}$  and  $^{59}\text{Co}$  [50]. The photoneutron cross section  $\sigma_{\gamma n}$  is converted to  $\gamma$  strength by the relation [51]

$$f(E_\gamma) = \frac{1}{3\pi^2\hbar^2c^2} \frac{\sigma_{(\gamma, n)}(E_\gamma)}{E_\gamma}. \quad (11)$$

The result is shown in figure 11, where we have compared with our normalizations for norm-1 and norm-2. We observe a very good agreement with the previous  $^3\text{He}$ -induced data below  $S_n$ , as well as with the ( $\gamma, n$ ) data.

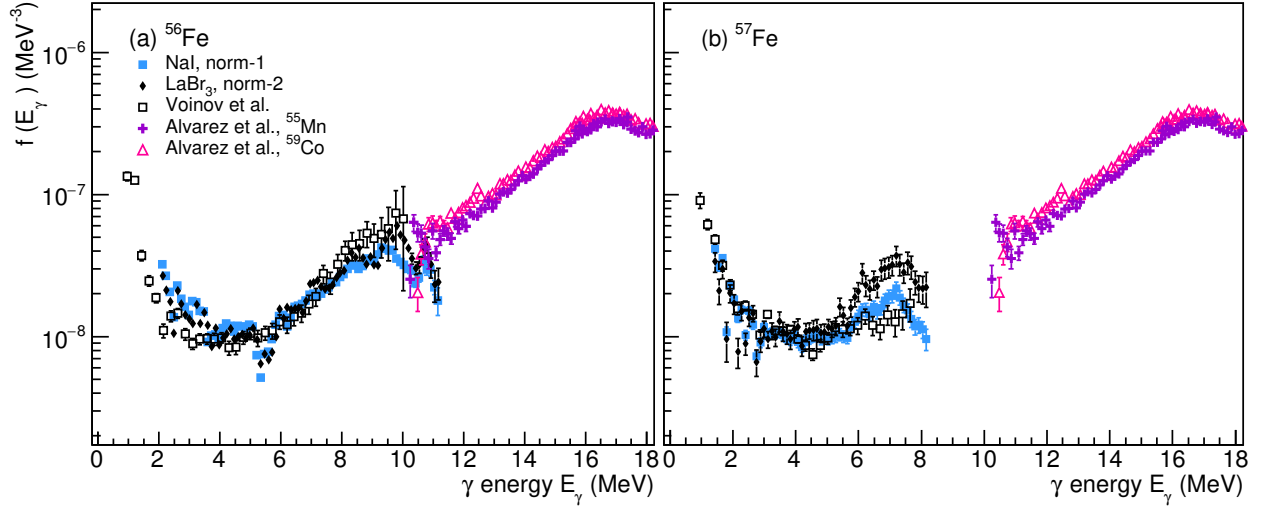


**Figure 11.** (Color online) Comparison of  $\gamma$ SFs from different reactions for (a)  $^{56}\text{Fe}$  and (b)  $^{56}\text{Fe}$ . Photonuclear data taken from [50]. For  $^{56}\text{Fe}$ , the present work provides the  $\gamma$ SF for  $2.1 \leq E_\gamma \leq 11.3$  MeV, while data from [6] cover  $1.0 \leq E_\gamma \leq 10.3$  MeV. Correspondingly, for  $^{57}\text{Fe}$ , the present work covers the range  $1.4 \leq E_\gamma \leq 8.2$  MeV, and data from [6]  $1.0 \leq E_\gamma \leq 7.6$  MeV. The photonuclear data [50] are for  $E_\gamma > 10.2$  MeV.

#### 4. Angular distributions, $^{57}\text{Fe}$

In [16], it was shown that the low-energy upbend in  $^{56}\text{Fe}$  is dominated by dipole transitions. Here, we apply the same type of analysis for the so-far unexplored  $^{57}\text{Fe}$  upbend.

We use the various angles  $\theta$  for which the NaI detectors are placed and extract angular distributions by sorting the data into  $(E_\gamma, E)$  matrices according to  $\theta$  of the NaI detectors relative to the beam direction. As the LaBr<sub>3</sub> detectors were placed at only four angles, and had a rather high  $E_\gamma$  threshold, these were not used for this analysis. From the intensities as a function of angle, we can fit angular-distribution functions of the form [52, 53]

$$W(\theta) = A_0 + A_2 P_2(\cos \theta) + A_4 P_4(\cos \theta), \quad (12)$$

where  $P_k(\cos \theta)$  is a Legendre polynomial of degree  $k$ , and we have

$$P_2(\cos \theta) = \frac{1}{2} [3(\cos \theta)^2 - 1], \quad (13)$$

$$P_4(\cos \theta) = \frac{1}{8} [35(\cos \theta)^4 - 30(\cos \theta)^2 + 3]. \quad (14)$$

The normalized angular-distribution coefficients are given by  $a_k = Q_k \alpha_k A_k / A_0$ , where  $Q_k \approx 1$  is the geometrical attenuation coefficient due to the finite size of the  $\gamma$  detectors, and  $\alpha_k$  is the attenuation due to partial alignment of the nuclei relative to the beam direction. We estimate uncertainties in the intensities according to



$\sigma_{\text{tot}}^{\text{err}} = \sigma_{\text{stat}}^{\text{err}} + \sigma_{\text{syst}}^{\text{err}}$ . The statistical errors are given by  $\sqrt{N}$  where  $N$  is the number of counts, and the systematic errors are deduced from the relative change in  $N$  for each symmetric pair of angles  $(37.4^\circ, 142.6^\circ)$ ,  $(63.4^\circ, 116.6^\circ)$ , and  $(79.3^\circ, 100.7^\circ)$ .

In the case of a fully aligned state with respect to the beam direction ( $\alpha_k = 1$ ), the  $a_k^{\text{max}}$  coefficients are given by [53]

$$a_k^{\text{max}}(J_i LL' J_f) = \frac{B_k}{1 + \delta^2} [F_k(J_f LL J_i) + 2\delta F_k(J_f LL' J_i) + \delta^2 F_k(J_f L' L' J_i)]. \quad (15)$$

Here,  $J_i, J_f$  are the spins of the initial and final level,  $L, L'$  are transition multipolarities,  $\delta$  is the mixing ratio between the multipolarities defined according to [54]:

$$\delta = \frac{\langle J_f || E(L+1) || J_i \rangle}{\langle J_f || M(L) || J_i \rangle}. \quad (16)$$

Here,  $E(L+1)$  is the electric transition operator for multipolarity  $L+1$ , and  $M(L)$  is the magnetic transition operator for multipolarity  $L$ . Further, the  $B_k, F_k$  coefficients are defined in [53], where also values for the product  $B_k F_k$  are tabulated.

First, we investigate known transitions in  $^{57}\text{Fe}$ , such as the 692-keV  $\gamma$  ray decaying from the level at 706 keV, where  $J_i = 5/2^-$  and  $J_f = 3/2^-$ , and the transition is known to be of  $M1 + E2$  type with a mixing ratio  $\delta = -0.465$  [55]. We get

$$a_2^{\text{max}} = \frac{1}{1 + 0.465^2} [B_2 F_2(3/2, 1, 1, 5/2) + 2 \cdot (-0.465) \cdot B_2 F_2(3/2, 1, 2, 5/2) + 0.465^2 B_2 F_2(3/2, 2, 2, 5/2)].$$

From [53] we have  $B_2 F_2(3/2, 1, 1, 5/2) = -0.400$ ,  $B_2 F_2(3/2, 1, 2, 5/2) = 1.014$ , and  $B_2 F_2(3/2, 2, 2, 5/2) = 0.204$ , giving  $a_2^{\text{max}} = -1.068$ . For  $a_4^{\text{max}}$ , we find

$$a_4^{\text{max}} = \frac{1}{1 + 0.465^2} [0.465^2 B_4 F_4(3/2, 2, 2, 5/2)];$$

with  $B_4 F_4(3/2, 2, 2, 5/2) = 0.653$ , we get  $a_4^{\text{max}} = 0.116$ . Similarly, we get for an  $E2$  transition with  $J_i = 9/2, J_f = 5/2$  and no mixing ( $\delta = 0$ ),  $a_2^{\text{max}} = 0.476$  and  $a_4^{\text{max}} = -0.286$ . In figure 12 we show the angular distributions of known transitions in  $^{57}\text{Fe}$ , and how they compare with the theoretical  $a_k^{\text{max}}$  values. All numbers are given in table 4. The comparison with the experimentally extracted  $a_2$  coefficients and the theoretical maximum values for the known transitions shown in figure 12a,b, indicates an attenuation  $\alpha_k \approx 0.6 - 0.75$ .

The behavior of the  $E_\gamma = 1261$  keV non-stretched $^\ddagger$   $M1 + E2$  transition is somewhat puzzling, as [55] gives a rather large mixing parameter of  $-0.35$  (see figure 12c). The shape of our data indicates a stronger contribution from the non-stretched  $M1$  part, although we do have a very large uncertainty in the  $a_4$  parameter. Nevertheless, assuming a pure  $M1$  transition, one finds  $a_2^{\text{max}} = 0.400$ , which is close to the experimental value of  $0.35(7)$ .

For the upbend, we have fitted equation 12 to the primary spectra for the range  $E = 5.4 - 7.6$  MeV and  $E_\gamma = 1.4 - 3.6$  MeV with  $a_2$  and  $a_4$  as free parameters,

$^\ddagger$  Transitions are called stretched for a maximum change in the angular momentum of the nuclear states, and non-stretched if the change is less than the maximum allowed for the given multipolarity.

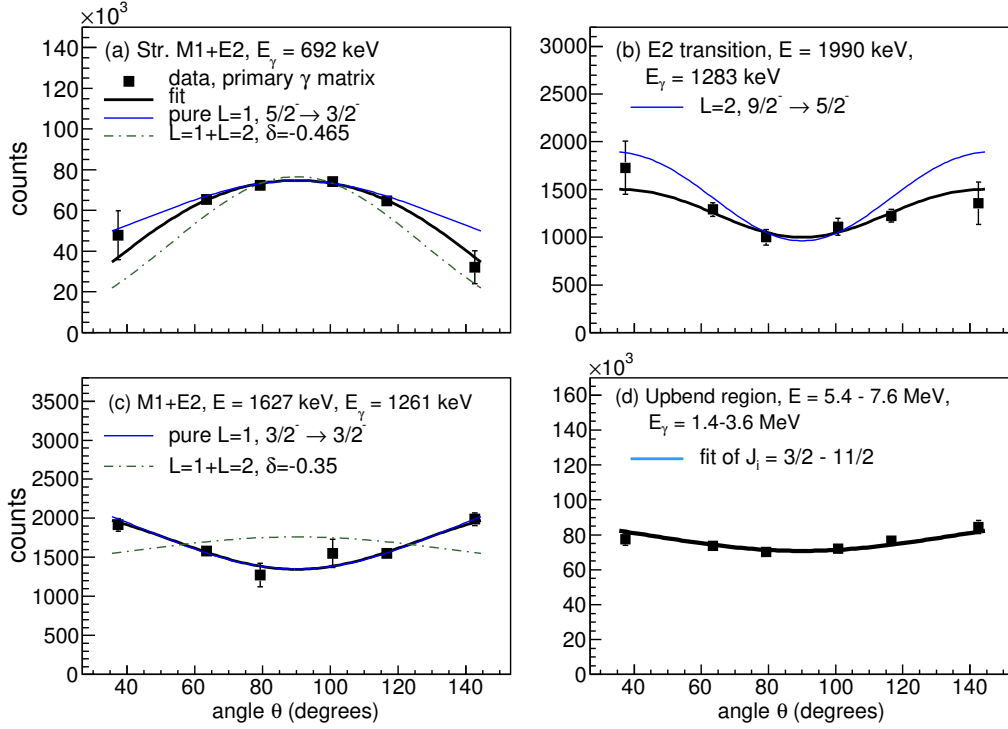


**Figure 12.** (Color online) Angular distributions for (a)–(c) single transitions and (d) the upbend region from primary transitions in  $^{57}\text{Fe}$ .

obtaining  $a_2 = 0.11(6)$  and  $a_4 = -0.06(6)$  (see figure 12d). The uncertainty in  $a_4$  is very large, but its value is small, indicating that contributions from stretched  $E2$  transitions are not dominant. Moreover, we have made a fit of the data to the sum of Legendre polynomials for  $J_i = 3/2 - 11/2$ , with a weighting coefficient for the stretched and the non-stretched part. Here, we obtain 78(16) and 34(10)% for the non-stretched and the stretched transitions, respectively. Note that possible contributions from other spins and  $E2$  transitions could modify these numbers, which should only be taken as a qualitative guidance. That said, the same trend was found in  $\langle B(M1) \rangle$  values from shell-model calculations of  $^{57}\text{Fe}$  [20], where non-stretched  $M1$  transitions contributed most to the low-energy enhancement. On the other hand, stretched  $M1$  transitions dominated both experimentally [16] and theoretically [20] in the case of  $^{56}\text{Fe}$ .

**Table 4.** Angular-distribution coefficients of transitions measured in the present experiment. The theoretical  $a_k^{\text{max}}$  coefficients for complete alignment are taken from Ref. [53].

$E$ (keV)	$E_\gamma$ (keV)	$I_i \rightarrow I_f$	$XL$	$\delta$	$a_2^{\text{max}}$	$a_2$	$a_4^{\text{max}}$	$a_4$
706	692	$5/2^- \rightarrow 3/2^-$	$M1 + E2$	-0.465	-1.068	-0.80(20)	0.12	-0.11(11)
1627	1261	$3/2^- \rightarrow 3/2^-$	$M1 + E2$	-0.35	-0.127	0.35(7)	0.00	-0.04(18)
1990	1283	$9/2^- \rightarrow 5/2^-$	$E2$	—	0.476	0.28(23)	-0.29	-0.20(20)

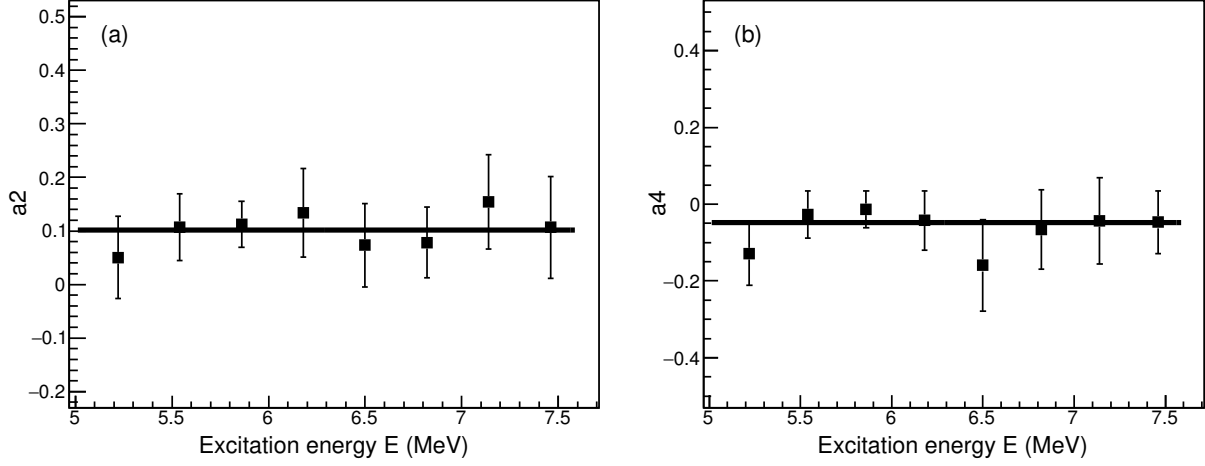


**Figure 13.** Extracted  $a_2$  and  $a_4$  coefficients from independent fits of 300-keV excitation-energy cuts in the  $^{57}\text{Fe}$  primary matrices for the six CACTUS angles.

To further study the angular-distribution coefficients for the upbend in  $^{57}\text{Fe}$  in more detail, we make individual fits of equation 12 to eight 300-keV wide excitation-energy cuts in the primary  $\gamma$ -ray matrix in the range  $E = 5.4 - 7.6$  MeV,  $E_\gamma = 1.4 - 3.6$  MeV. The resulting  $a_2$  and  $a_4$  coefficients are shown in figure 13. We obtain  $a_2 = 0.10(3)$  and  $a_4 = -0.05(3)$ , in excellent agreement with the simultaneous fit to the whole region as shown in figure 12d. Hence, we conclude that the upbend structure in  $^{57}\text{Fe}$  is also very likely to be caused by dipole transitions, but for this case the non-stretched transitions seem to dominate.

## 5. Generalized Brink-Axel hypothesis: $\gamma\text{SF}$ as function of excitation energy

As the LaBr<sub>3</sub> detectors have excellent energy resolution and efficiency for high-energy  $\gamma$  rays, we make use of the technique described in [11, 21, 56] to extract the  $\gamma\text{SF}$  as function of excitation energy.

We start with the primary  $\gamma$ -ray matrix  $P(E_\gamma, E)$  obtained in section 2. We will now make the assumption that the NLD is the one determined in section 3, but the transmission coefficient  $\mathcal{T}$  is now allowed to be dependent on both excitation energy and  $\gamma$ -ray energy,  $\mathcal{T}(E_\gamma, E)$ . As  $\rho(E_f)$  is known, we can in principle determine  $\mathcal{T}(E_\gamma, E)$  for each excitation-energy bin just by dividing the primary  $\gamma$  matrix with the NLD:  $\mathcal{T}(E_\gamma, E) \sim P(E_\gamma, E)/\rho(E_f)$ , using our ansatz in equation 2. Specifically, we have

$$\rho(E - E_\gamma)\mathcal{T}(E_\gamma, E) = N(E)P(E_\gamma, E), \quad (17)$$

where  $N(E)$  is a normalization factor in units  $\text{MeV}^{-1}$ , depending only on the initial excitation energy.

Now, this game can be played in two ways:

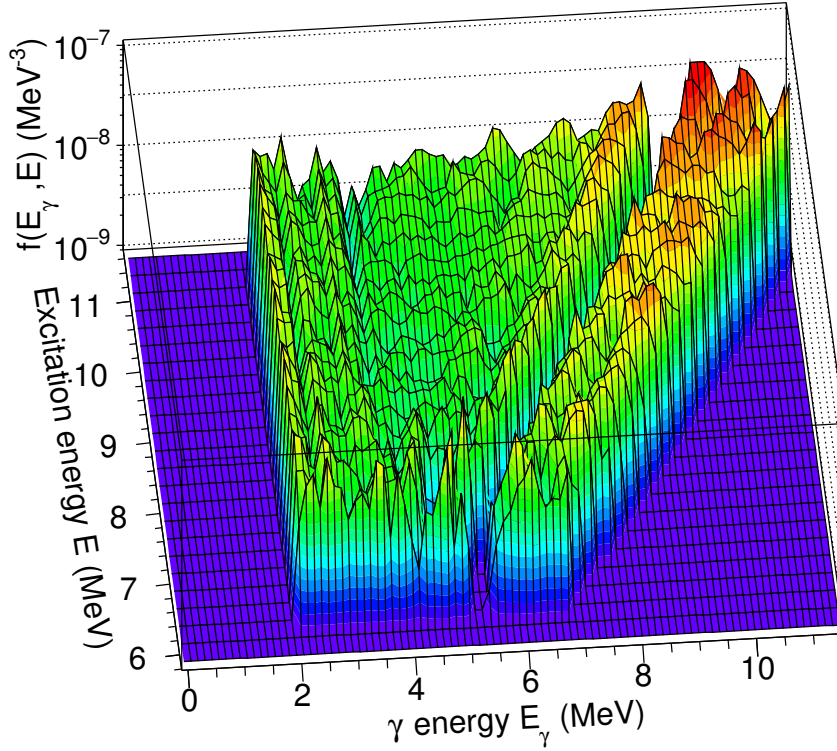


**Figure 14.** (Color online) Extracted  $\gamma$ SFs as function of initial excitation energy for  $^{56}\text{Fe}$ . Bins are 248 keV/channel for  $E$  and 124 keV/channel for  $E_\gamma$ .

- (a) We investigate  $\mathcal{T}$  as function of *initial* excitation energy through the relation

$$\mathcal{T}(E_\gamma, E) = N(E) \frac{P(E_\gamma, E)}{\rho(E - E_\gamma)}. \quad (18)$$

We determine  $N(E)$  by

$$N(E) = \frac{\int_0^E \mathcal{T}(E_\gamma) \rho(E - E_\gamma) dE_\gamma}{\int_0^E P(E_\gamma, E) dE_\gamma}. \quad (19)$$

Note that  $\mathcal{T}(E_\gamma)$  is the normalized transmission coefficient from section 3. However, it will not influence the *shape* of the extracted  $\mathcal{T}(E_\gamma, E)$  as it acts as a constant after integrating over all  $E_\gamma$ . Hence, it only serves to provide an approximate absolute normalization of  $\mathcal{T}(E_\gamma, E)$ .

- (b) We can also find  $\mathcal{T}$  as function of *final* excitation energy by

$$\mathcal{T}(E_\gamma, E_f) = N(E_\gamma + E_f) \frac{P(E_\gamma, E_f + E_\gamma)}{\rho(E_f)}, \quad (20)$$

where we keep in mind that  $E_f + E_\gamma = E$ . Again, we assume that  $\mathcal{T}(E_\gamma)$  gives a good estimate of the absolute value and we can approximate the normalization for

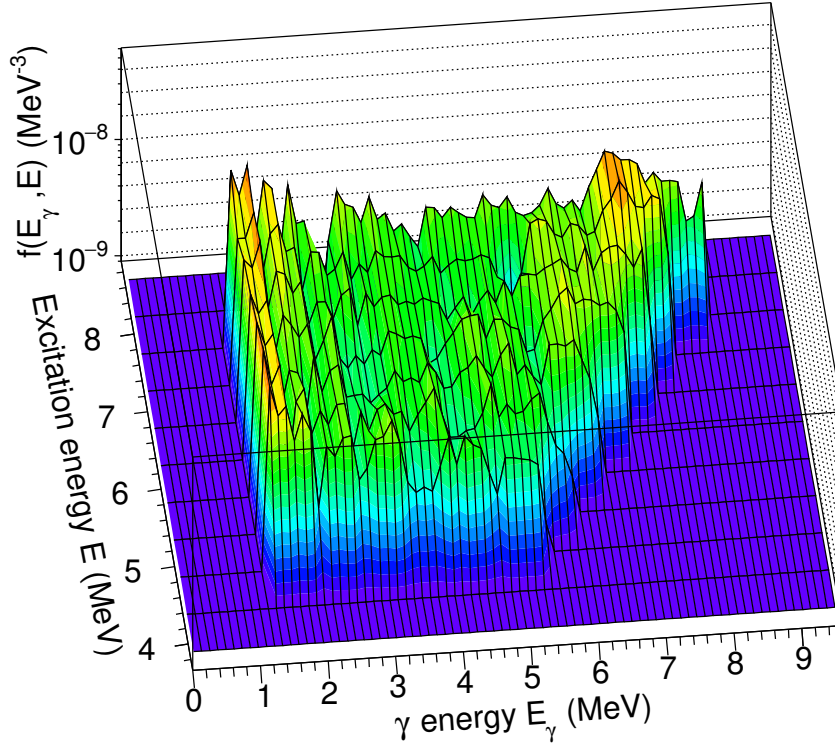


**Figure 15.** (Color online) Extracted  $\gamma$ SFs as function of initial excitation energy for  $^{57}\text{Fe}$ . Bins are 480 keV/channel for  $E$  and 120 keV/channel for  $E_\gamma$ .

a given final excitation energy  $E_f$  and for a specific  $E_\gamma$  fulfilling  $E = E_f + E_\gamma$  by

$$N(E_\gamma + E_f) = \frac{\int_0^{E_f+E_\gamma} \mathcal{T}(E'_\gamma) \rho(E_f) dE'_\gamma}{\int_0^{E_f+E_\gamma} P(E'_\gamma, E_f + E_\gamma) dE'_\gamma}. \quad (21)$$

The  $\gamma$ SF as function of excitation energy is then easily calculated from the transmission coefficient by use of equation 10. The results are shown for  $^{56,57}\text{Fe}$  in figures 14 and 15, respectively.

We observe that the decay strength to the ground state increases as function of both  $E$  and  $E_\gamma$ , which is fully consistent with the  $\gamma$ SF determined previously in section 3 and the expected influence of the tail from the GDR. Moreover, we find that the  $\gamma$ SF varies with initial excitation energy, but that the general shape is preserved: there is always an upbend at low  $E_\gamma$  and a rather flat distribution of strength in the middle  $E_\gamma$  region, before it again increases for high  $E_\gamma$ .

To investigate the fluctuations, following [56], we compare the average  $\gamma$ SF for all initial excitation energies with the  $\gamma$ SF obtained for a specific excitation-energy bin. We find that the fluctuations relative to the average  $\gamma$ SF can be large, more than 100% for some  $\gamma$ -ray energies and  $E$ . Also, the fluctuations are in some cases significantly larger than the error bars. Therefore, it seems that although the overall shape of the

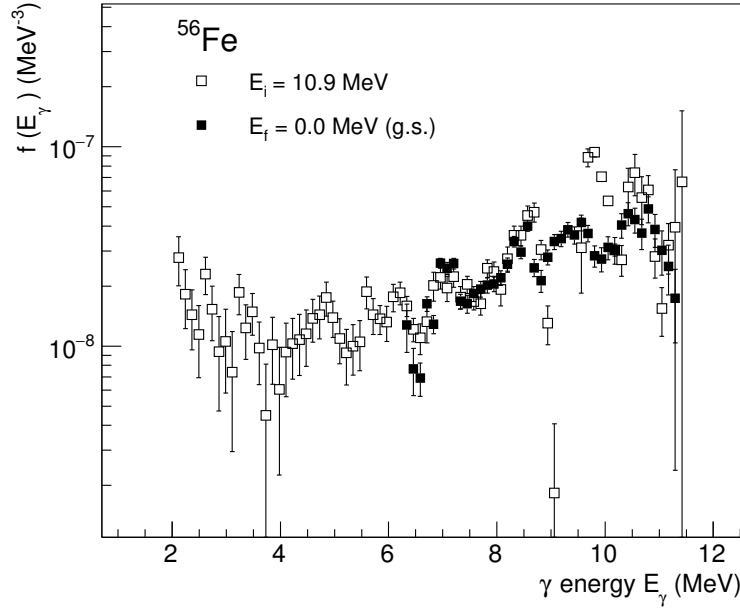


**Figure 16.** Extracted  $\gamma$ SF for the  $^{56}\text{Fe}$  ground state as  $E_f$  (black points) and for  $E = 10.9$  MeV.

$\gamma$ SF is indeed preserved in agreement with the generalized Brink-Axel hypothesis, the  $\gamma$ SF for a specific transition energy and excitation energy could have a large deviation, in particular when the excitation-energy bin is narrow and containing rather few levels.

Finally, we also investigate the  $\gamma$ SF for a specific final excitation energy. We have chosen the ground state in  $^{56}\text{Fe}$  and the ground-state band ( $1/2^-$ ,  $3/2^-$ ,  $5/2^-$ ) in  $^{57}\text{Fe}$ . The  $\gamma$ SF for this  $E_f$  is then compared to a typical  $\gamma$ SF at a high initial  $E$ , see figures 16 and 17. Again, we observe that the general trend is preserved, although significant deviations are present, for example for the  $^{56}\text{Fe}$  strength at  $E_\gamma \approx 9.7$  MeV. This is interpreted to be caused by Porter-Thomas fluctuations, which are expected to be large when the final and/or the initial NLD is low [21].

## 6. Summary and outlook

In this work, we have presented data on  $^{56,57}\text{Fe}$  from  $(p, p'\gamma)$  reactions, measuring the  $\gamma$  rays both with NaI and LaBr<sub>3</sub> crystals. From the sets of particle- $\gamma$  coincidences, we have extracted NLDs and  $\gamma$ SFs for these nuclei. We find that our present results compare well with previous measurements.

We have measured angular distributions for  $^{57}\text{Fe}$ , and we get coefficients in agreement with a dominance of non-stretched dipoles for the upbend, in agreement with recent shell-model calculations. Moreover, we have investigated the excitation-energy dependence of the  $\gamma$ SF. The data show that the general trends are preserved, i.e.

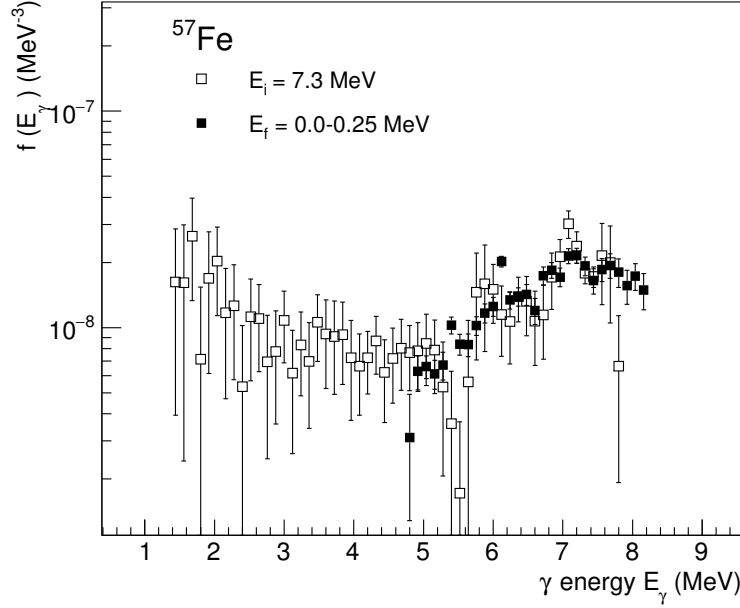


**Figure 17.** Extracted  $\gamma$ SF for the  $^{57}\text{Fe}$  ground-state band,  $E_f = 0.0 - 0.25$  MeV (black points) and for  $E_i = 7.3$  MeV.

the upbend and an enhanced decay strength for high-energy transitions, in accordance with the Brink-Axel hypothesis. However, we also encounter large fluctuations, which seem to be due to strong Porter-Thomas fluctuations caused by the low level density in these light nuclei.

## Acknowledgments

The authors wish to thank J.C. Müller, E.A. Olsen, A. Semchenkov and J. C. Wikne at the Oslo Cyclotron Laboratory for providing excellent experimental conditions. This work was financed by the Research Council of Norway (NFR), project grant no. 205528, and through ERC-STG-2014 under grant agreement no. 637686. S. S. and G. M. T. acknowledge financial support by the NFR under project grant no. 210007 and 222287, respectively. A. V. V. acknowledges funding from the Department of Energy, grant no. DE-NA0002905. M. W. acknowledges support by the National Research Foundation of South Africa under grant no. 92789.

## References

- [1] Arnould M and Goriely S 2003 *Phys. Rep.* **384** 1
- [2] Arnould M, Goriely S, and Takahashi K 2007 *Phys. Rep.* **450** 97
- [3] Aliberti G, Palmiotti G, Salvatores M, and Stenberg C G 2004 *Nucl. Sci. Eng.* **146** 13
- [4] Aliberti G *et al.* 2006 *Ann. Nucl. Energy* **33** 13



- [5] Schiller A, Bergholt L, Guttormsen M, Melby E, Rekstad J, and Siem S 2000 *Nucl. Instrum. Methods Phys. Res. A* **447** 498
- [6] Voinov A *et al.* 2004 *Phys. Rev. Lett.* **93** 142504
- [7] Larsen A C *et al.* 2007 *Phys. Rev. C* **76** 044303
- [8] Bürger A *et al.* 2012 *Phys. Rev. C* **85** 064328
- [9] Voinov A V *et al.* 2010 *Phys. Rev. C* **81** 024319
- [10] Renstrøm T *et al.* 2016 *Phys. Rev. C* **93** 064302
- [11] Guttormsen M *et al.* 2005 *Phys. Rev. C* **71** 044307
- [12] Wiedeking M *et al.* 2012 *Phys. Rev. Lett.* **108** 162503
- [13] Tveten G M *et al.* 2016 *Phys. Rev. C* **94** 025804
- [14] Kheswa B V *et al.* 2015 *Phys. Lett. B* **744** 268
- [15] Simon A *et al.* 2016 *Phys. Rev. C* **93** 034303
- [16] Larsen A C *et al.* 2013 *Phys. Rev. Lett.* **111** 242504
- [17] Larsen A C and Goriely S 2010 *Phys. Rev. C* **82** 014318
- [18] Litvinova E and Belov N 2013 *Phys. Rev. C* **88** 031302(R)
- [19] Schwengner R, Frauendorf S, and Larsen A C 2013 *Phys. Rev. Lett.* **111** 232504
- [20] Brown B A and Larsen A C 2014 *Phys. Rev. Lett.* **113** 252502
- [21] Guttormsen M *et al.* 2016 *Phys. Rev. Lett.* **116** 012502
- [22] Guttormsen M, Bürger A, Hansen T E, and Lietaer N 2011 *Nucl. Instrum. Methods Phys. Res. A* **648** 168
- [23] Guttormsen M *et al.* 1990 *Phys. Scr. T* **32** 54
- [24] Nicolini R *et al.* 2007 *Nucl. Instrum. Methods Phys. Res. A* **582** 554
- [25] Giaz A *et al.* 2013 *Nucl. Instrum. Methods Phys. Res. A* **729** 910
- [26] Wiedeking M *et al.* 2016 *Phys. Rev. C* **93** 024303
- [27] Guttormsen M *et al.* 1996 *Nucl. Instrum. Methods Phys. Res. A* **374** 371
- [28] Crespo Campo L *et al.* 2016 *Phys. Rev. C* (in press)
- [29] Guttormsen M, Ramsøy T, and Rekstad J 1987 *Nucl. Instrum. Methods Phys. Res. A* **255** 518
- [30] Dirac P A M 1927 *Proc. R. Soc. London A* **114** 243
- [31] Fermi E 1950 *Nuclear Physics* (University of Chicago Press, Chicago)
- [32] Brink D M 1955 *Dr. Phil. thesis, Oxford University*
- [33] Axel P 1962 *Phys. Rev.* **126** 671
- [34] Bohr A and Mottelson B 1969 *Nuclear Structure* (Benjamin, New York, Vol. I)
- [35] Larsen A C *et al.* 2011 *Phys. Rev. C* **83** 034315
- [36] Porter C E and Thomas R G 1956 *Phys. Rev.* **104** 483
- [37] Data from the NNDC On-Line Data Service database as of August 2016; available at <http://www.nndc.bnl.gov/nudat2/>
- [38] Capote R *et al.* 2009 *Nucl. Data Sheets* **110** 3107; *Reference Input Parameter Library (RIPL-3)*, available at <http://www-nds.iaea.org/RIPL-3/>
- [39] Larsen A C *et al.* 2016 *Phys. Rev. C* **93** 045810
- [40] von Egidy T and Bucurescu D 2009 *Phys. Rev. C* **80** 054310
- [41] von Egidy T and Bucurescu D 2005 *Phys. Rev. C* **72** 044311; 2006 *Phys. Rev. C* **73** 049901(E)
- [42] Ericson T 1959 *Nucl. Phys.* **11** 481
- [43] Ericson T 1960 *Adv. Phys.* **9** 425
- [44] Voinov A, Guttormsen M, Melby E, Rekstad J, Schiller A, and Siem S 2001 *Phys. Rev. C* **63** 044313
- [45] Kopecky J and Uhl M 1990 *Phys. Rev. C* **41** 1941
- [46] Voinov A *et al.* 2006 *Phys. Rev. C* **74** 014314
- [47] Vonach H K *et al.* 1966 *Phys. Rev.* **149** 844
- [48] Voinov A *et al.* 2007 *Phys. Rev. C* **76** 044602
- [49] Fischer F F *et al.*, *Phys. Rev. C* **30**, 72 (1984)
- [50] Alvarez R A, Berman B L, Faul D D, Lewis Jr F H, and Meyer P 1979 *Phys. Rev. C* **20** 128

- [51] Bartholomew G A, Earle E D, Ferguson A J, Knowles J W, and Lone M A 1972 *Adv. Nucl. Phys.* **7** 229
- [52] Litherland A E and A. J. Ferguson A J 1961 *Can. J. Phys.* **39** 788
- [53] der Mateosian E and Sunyar A W 1974 *At. Data and Nucl. Data Tables* **13** 391
- [54] Krane K S 1978 *At. Data and Nucl. Data Tables* **22** 269
- [55] Data from the Evaluated Nuclear Structure Data File (ENSDF) as of August 2016, available at <http://www.nndc.bnl.gov/ensdf/>
- [56] Guttormsen M *et al.* 2011 *Phys. Rev. C* **83** 014312